

Article

Elastic Properties of Orthorhombic $\text{YBa}_2\text{Cu}_3\text{O}_7$ under Pressure

Cai Chen ^{1,2,*}, Lili Liu ^{2,3}, Yufeng Wen ^{4,5}, Youchang Jiang ² and Liwan Chen ²¹ College of Civil Engineering, Chongqing Three Gorges University, Chongqing 404100, China² Department of Physics, Chongqing Three Gorges University, Chongqing 404100, China³ Institute for Structure and Function, Chongqing University, Chongqing 401331, China⁴ School of Mathematical Sciences and Physics, Jinggangshan University, Ji'an 343009, China⁵ School of Materials Science and Engineering, Shanghai Jiaotong University, Shanghai 200240, China

* Correspondence: chencai0612@163.com

Received: 1 September 2019; Accepted: 19 September 2019; Published: 25 September 2019



Abstract: The pressure dependence of the lattice and elastic constants of the orthorhombic $\text{YBa}_2\text{Cu}_3\text{O}_7$ are firstly investigated using the first principles calculations based on the density functional theory. The calculated lattice parameters at 0 GPa are in agreement with the available experimental data. By the elastic stability criteria under isotropic pressure, it is predicted that $\text{YBa}_2\text{Cu}_3\text{O}_7$ with and orthorhombic structure is mechanically stable under pressure up to 100 GPa. On the basis of the elastic constants, Pugh's modulus ratio, Poisson's ratio, elastic anisotropy, Debye temperature, and the minimum thermal conductivity of $\text{YBa}_2\text{Cu}_3\text{O}_7$ under pressure up to 100 GPa are further investigated. It is found that its ductility, Debye temperature, and minimum thermal conductivity increase with pressure.

Keywords: orthorhombic $\text{YBa}_2\text{Cu}_3\text{O}_7$; structural stability; elastic properties; pressure; first principles

1. Introduction

The discovery of the Ba-La-Cu-O system by Bednorz and Müller [1] with a superconducting transition temperature of 30 K has generated a great deal of tremendous interest among physicists and material scientists and sparked intensive studies of the cuprate systems. Further research has led Wu et al. [2] to the discovery of a superconducting transition temperature of 90 K in the multiphase Y-Ba-Cu-O system. One of the best-studied superconductors is nearly stoichiometric $\text{YBa}_2\text{Cu}_3\text{O}_7$. $\text{YBa}_2\text{Cu}_3\text{O}_7$ has the $Pmma$ space group, and its crystal structure is shown in Figure 1. There are thirteen atoms per primitive cell. This compound has a high superconducting transition temperature and a relatively simple structure, and much research is focused on this superconductor [3–7]. For example, Murakami et al. [8] used a standard vibrating sample magnetometer equipped with a cryostat to measure the magnetization of $\text{YBa}_2\text{Cu}_3\text{O}_7$ samples fabricated by the quench and melt growth (QMG) technique, and they found that the magnetization behavior of QMG-processed $\text{YBa}_2\text{Cu}_3\text{O}_7$ can be understood in terms of the Bean critical state model. Fong et al. [9] reported inelastic neutron scattering measurements at excitation energies $\hbar\omega \sim 41$ meV in $\text{YBa}_2\text{Cu}_3\text{O}_7$, and their results indicated that magnetic scattering centered around 41 meV and $\mathbf{q} = (\pi/a, \pi/a)$ appears in the superconducting state only. Sánchez-Vald e et al. [10] studied the nucleation, growth, and sintering stages of epitaxial $\text{YBa}_2\text{Cu}_3\text{O}_{6+\delta}$ superconducting thin films by means of in situ electrical measurements. Dadras et al. [11] investigated the effects of three samples of carbon-based nanostructure doping on the properties of the $\text{YBa}_2\text{Cu}_3\text{O}_{7-\delta}$ high-temperature superconductor, and they found that carbon nanostructures such as C, SiC, and CNT can improve the critical current density of $\text{YBa}_2\text{Cu}_3\text{O}_{7-\delta}$. Horide [12] researched the influence of the matching field on the critical current density and

irreversibility temperature in $\text{YBa}_2\text{Cu}_3\text{O}_7$ films containing BaMO_3 ($M = \text{Zr}, \text{Sn}, \text{Hf}$) nanorods. Hapipi et al. [13] investigated the effect of the calcination process (single and multiple calculations) on the nominal composition $\text{YBa}_2\text{Cu}_3\text{O}_{7-\delta}$ (γ -123) by using the four-point temperature resistance measurement, X-ray diffraction (XRD), and field-emission scanning electron microscopy (FESEM). All this research is mainly focused on experimental research, and the results are very important to further scientific and technical investigations. However, there is almost no theoretical research on the orthorhombic $\text{YBa}_2\text{Cu}_3\text{O}_7$, and the elastic properties of $\text{YBa}_2\text{Cu}_3\text{O}_7$ under pressure have received little attention.

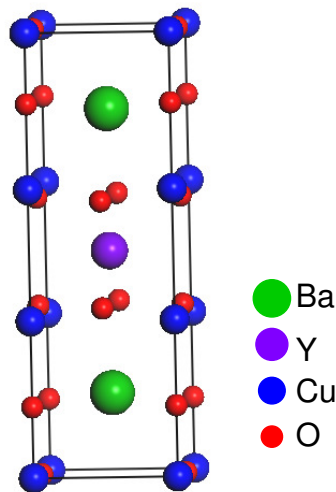


Figure 1. The conventional unit cell of $\text{YBa}_2\text{Cu}_3\text{O}_7$.

As is known, elastic properties are closely associated with many fundamental solid-state properties, such as bulk modulus, shear modulus, Young's modulus, thermal expansion, Debye temperature, minimum thermal conductivity, etc. Besides, many practical applications related to the mechanical properties can be deduced from the elastic constants, for example load deflection, internal strain, and fracture toughness [14]. Single-crystal elastic constants at lower pressure for $\text{YBa}_2\text{Cu}_3\text{O}_7$ are scarce in literature due to the difficulties of the experiments, let alone the elastic constants at higher pressure. Besides, the pressure-induced structural phase transitions can be predicted from the elastic constants under different pressures. Hence, in this work, we pay close attention to the elastic properties of $\text{YBa}_2\text{Cu}_3\text{O}_7$ under pressure up to 100 GPa by using the first principles calculations. The rest of the paper is organized as follows. The theory and computational details based on the first principles methods are given in Section 2. Some results and discussion under pressure are presented in Section 3. Finally, the conclusions are drawn in Section 4.

2. Theory and Computational Details

In this work, the first principles calculations based on density functional theory (DFT) are performed by employing the plane wave basis projector augmented wave (PAW) method [15,16], as implemented in the VASPcode [17–19]. The exchange-correlation functional for all elements is described with the generalized gradient approximation (GGA) of Perdew–Burke–Ernzerhof (PBE) [20]. A plane-wave energy cutoff of 500 eV was employed throughout the calculations. The convergence of energy and force were set to 10^{-6} eV and 10^{-4} eV/Å, respectively. The k -point meshes for Brillouin zone integrations were performed using the γ -centered Monkhorst–Pack scheme [21], and the $11 \times 11 \times 5$ k -point grids were used. The crystal at the given pressure is fully relaxed with respect to the volume, shape, and internal atomic positions until the change in the total energy is smaller than

10^{-5} eV between two ionic step relaxations, and then, the lattice parameters under different pressures are determined.

We used the strain energy–strain curve to calculate the elastic constants. For $\text{YBa}_2\text{Cu}_3\text{O}_7$ with the orthorhombic structure, there are nine independent elastic constants c_{11} , c_{12} , c_{13} , c_{22} , c_{23} , c_{33} , c_{44} , c_{55} , and c_{66} . To calculate the complete elastic constants, the nine Lagrangian strain tensors in terms of a parameter γ listed in Table 1 were introduced. For each strain, γ was varied between -0.02 and 0.02 with step 0.002 , that is we needed to calculate the total strain energies of the 21 points for each strain tensor. The calculated $E - \gamma$ points were then fitted to the least-squares polynomial, and the elastic constants could be concluded from the second-order derivatives of E with respect to γ . Details of the calculations were introduced in [22].

Based on the Voigt–Reuss–Hill approximation, other mechanical parameters for polycrystalline aggregates such as the bulk modulus B , shear modulus G , Poisson’s ratio ν , and Vickers’ hardness H_v can be obtained via the elastic constants. According to the Voigt and Reuss approximation, the bulk modulus and shear modulus for orthorhombic crystals can be written as [23–25]:

$$\begin{aligned}
 B_V &= \frac{1}{9}(c_{11} + 2c_{12} + 2c_{13} + c_{22} + 2c_{23} + c_{33}) \\
 B_R &= \chi \left[c_{11}(c_{22} + c_{33} - 2c_{23}) + c_{22}(c_{33} - 2c_{13}) - 2c_{33}c_{12} \right. \\
 &\quad \left. + c_{12}(2c_{23} - c_{12}) + c_{13}(2c_{12} - c_{13}) + c_{23}(2c_{13} - c_{23}) \right]^{-1} \\
 G_V &= \frac{1}{15}(c_{11} - c_{12} - c_{13} + c_{22} - c_{23} + c_{33} + 3c_{44} + 3c_{55} + 3c_{66}) \\
 G_R &= 15 \left\{ 4[c_{11}(c_{22} + c_{33} + c_{23}) + c_{22}(c_{33} + c_{13} + c_{33}c_{12} - c_{12}(c_{23} + c_{12}) \right. \\
 &\quad \left. c_{13}(c_{12} + c_{13}) - c_{23}(c_{13} + c_{23})] / \chi + 3(c_{44}^{-1} + c_{55}^{-1} + c_{66}^{-1}) \right\}^{-1}
 \end{aligned} \tag{1}$$

with:

$$\chi = c_{13}(c_{12}c_{23} - c_{13}c_{22}) + c_{23}(c_{12}c_{13} - c_{23}c_{11}) + c_{33}(c_{11}c_{22} - c_{12}^2) \tag{2}$$

Using the Hill model, the shear modulus and the bulk modulus are the arithmetic averages of Voigt and Reuss bounds [26], that is:

$$\begin{aligned}
 B &= \frac{B_V + B_R}{2} \\
 G &= \frac{G_V + G_R}{2}
 \end{aligned} \tag{3}$$

Table 1. The relationship between the Lagrangian strain and the corresponding coefficient.

Strain Type	Λ
$A_1 = (\gamma, 0, 0, 0, 0, 0)$	c_{11}
$A_2 = (0, \gamma, 0, 0, 0, 0)$	c_{12}
$A_3 = (0, 0, \gamma, 0, 0, 0)$	c_{33}
$A_4 = (\gamma, \gamma, 0, 0, 0, 0)$	$c_{11} + c_{22} + 2c_{12}$
$A_5 = (\gamma, 0, \gamma, 0, 0, 0)$	$c_{11} + c_{33} + 2c_{13}$
$A_6 = (0, \gamma, \gamma, 0, 0, 0)$	$c_{22} + c_{33} + 2c_{23}$
$A_7 = (\gamma, 0, 0, 2\gamma, 0, 0)$	$c_{11} + 4c_{44}$
$A_8 = (\gamma, 0, 0, 0, 2\gamma, 0)$	$c_{11} + 4c_{55}$
$A_9 = (\gamma, 0, 0, 0, 0, 2\gamma)$	$c_{11} + 4c_{66}$

3. Results and Discussion

3.1. Structure and Elastic Properties of $\text{YBa}_2\text{Cu}_3\text{O}_7$ under Different Pressures

The lattice parameters and density of $\text{YBa}_2\text{Cu}_3\text{O}_7$ under pressure up to 100 GPa were firstly calculated, and the results are summarized in Table 2. Using high-resolution neutron powder diffraction, Beno et al. [27] determined the lattice constants of $\text{YBa}_2\text{Cu}_3\text{O}_7$ to be $a = 3.8231 \text{ \AA}$, $b = 3.8864 \text{ \AA}$, and $c = 11.6807 \text{ \AA}$, and from powder X-ray diffraction data, Cava et al. [28] proposed the unit cell of $\text{YBa}_2\text{Cu}_3\text{O}_7$ with $a \approx 3.822 \text{ \AA}$, $b \approx 3.891 \text{ \AA}$, $c \approx 11.677 \text{ \AA}$. The difference between our results and experimental data were less than 1.5%, indicating that the computational methodology employed in the present work was reliable. Unfortunately, no experimental and theoretical values of the lattice parameters under high pressure are available for comparison. Furthermore, the pressure-dependent lattice parameters a/a_0 , b/b_0 , c/c_0 , V/V_0 (where a_0 , b_0 , c_0 , and V_0 are the equilibrium structure parameters and cell volume at 0 GPa) are plotted in Figure 2. It can be found that a/a_0 , b/b_0 , and c/c_0 decreased with increasing pressure, and the decreasing rate of c/c_0 was much larger than those of a/a_0 and b/b_0 , while a and b axes nearly had the same decreasing rate. Hence, it can be concluded that the c axis was most easily compressed.

Table 2. Calculated lattice parameters (a , b , c in \AA) and primitive cell volume (V in \AA^3) of $\text{YBa}_2\text{Cu}_3\text{O}_7$ under pressure up to 100 GPa.

P	a	b	c	V
0	3.853	3.936	11.822	179.266
10	3.781	3.866	11.362	166.072
20	3.727	3.809	11.057	157.016
30	3.688	3.763	10.802	149.923
40	3.659	3.723	10.575	144.047
50	3.635	3.689	10.367	138.996
60	3.614	3.658	10.183	134.627
70	3.593	3.631	10.028	130.839
80	3.574	3.605	9.898	127.517
90	3.555	3.581	9.785	124.563
100	3.538	3.558	9.685	121.904

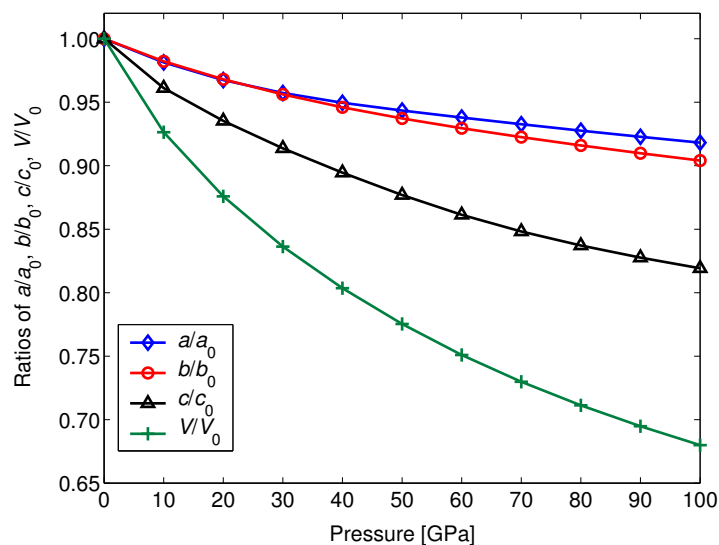


Figure 2. Pressure-dependent normalized parameters a/a_0 , b/b_0 , c/c_0 , and V/V_0 of $\text{YBa}_2\text{Cu}_3\text{O}_7$.

Knowledge of the elastic constants is significant for understanding the structural stability and mechanical properties of a crystal. Table 3 gives the calculated elastic constants under different

pressures. The present results at ground state ($c_{11} = 223.94$ GPa, $c_{12} = 103.59$ GPa, $c_{13} = 54.34$ GPa, $c_{22} = 233.04$ GPa, $c_{23} = 66.76$ GPa, $c_{33} = 200.46$ GPa, $c_{44} = 55.83$ GPa, $c_{55} = 47.77$ GPa, $c_{66} = 81.49$ GPa) nearly agreed well with the experimental results at room temperature ($c_{11} = 231$ GPa, $c_{12} = 132$ GPa, $c_{13} = 71$ GPa, $c_{22} = 268$ GPa, $c_{23} = 95$ GPa, $c_{33} = 186$ GPa, $c_{44} = 49$ GPa, $c_{55} = 37$ GPa, $c_{66} = 95$ GPa) obtained using resonant ultrasound spectroscopy [29]. For the orthorhombic crystals, the mechanical stability criterion under hydrostatic pressure can be written as: [30]

$$\begin{aligned} \tilde{c}_{11} + \tilde{c}_{22} - 2\tilde{c}_{12} > 0, \quad \tilde{c}_{11} + \tilde{c}_{33} - 2\tilde{c}_{13} > 0, \quad \tilde{c}_{22} + \tilde{c}_{33} - 2\tilde{c}_{23} > 0 \\ \tilde{c}_{ii} > 0 \quad (i = 1 \sim 6) \\ \tilde{c}_{11} + \tilde{c}_{22} + \tilde{c}_{33} + 2\tilde{c}_{12} + 2\tilde{c}_{13} + 2\tilde{c}_{23} > 0 \end{aligned} \quad (4)$$

where $\tilde{c}_{ii} = c_{ii} - P$ ($i = 1 \sim 6$), $\tilde{c}_{12} = c_{12} + P$, $\tilde{c}_{13} = c_{13} + P$, $\tilde{c}_{23} = c_{23} + P$. The elastic constants under different pressures obey these stability criteria, implying that the orthorhombic $\text{YBa}_2\text{Cu}_3\text{O}_7$ is mechanically stable within 100 GPa. As can be seen from Table 3, all the elastic constants increased monotonically with pressure. c_{11} , c_{22} , and c_{33} represent the resistance to linear compression, and the other elastic constants are mainly associated with the elasticity in shape. In the entire pressure range of our calculations, c_{11} , c_{22} , and c_{33} were much larger than those of the other elastic constants, indicating that the deformation resistances of $\text{YBa}_2\text{Cu}_3\text{O}_7$ along the axial directions were stronger than those of the non-axial directions. Further, the relationship $c_{22} > c_{11} > c_{33}$ under different pressures implied that the strength of the bonding along the [010] direction was stronger than those along the [100] and [001] directions.

Table 3. Calculated elastic constants c_{ij} (GPa) of $\text{YBa}_2\text{Cu}_3\text{O}_7$ under pressure up to 100 GPa.

Pressure	c_{11}	c_{12}	c_{13}	c_{22}	c_{23}	c_{33}	c_{44}	c_{55}	c_{66}
0	223.94	103.59	54.34	233.04	66.76	200.46	55.83	47.77	81.49
10	294.84	139.59	88.79	307.70	94.57	273.90	68.35	64.87	98.58
20	358.75	170.78	121.11	382.88	117.58	341.29	78.54	79.73	112.23
30	428.73	199.44	153.03	456.43	141.42	400.82	87.52	93.84	123.55
40	494.09	226.48	184.12	528.66	163.74	459.66	95.99	108.19	133.67
50	552.74	252.19	219.21	598.64	186.13	514.81	104.46	122.77	143.67
60	617.40	277.96	248.37	667.18	209.66	571.45	112.57	137.91	151.62
70	674.69	303.17	276.99	730.31	232.24	626.35	120.98	152.54	159.69
80	728.53	327.65	309.33	791.69	256.01	678.79	128.91	166.80	168.13
90	780.14	349.91	344.51	850.17	283.01	724.34	136.50	180.76	176.64
100	826.38	376.19	379.47	903.90	310.53	769.85	143.76	194.39	185.41

The bulk modulus B describes the resistance to volume (bond-length) change, and the shear modulus G represents the resistance to shape (bond-angle) change with applied stress, respectively. Generally, a material presents more ductility if it has a larger bulk modulus and a smaller shear modulus. The pressure dependence of B and G is plotted in Figure 3a. It can be seen that both B and G increased with increasing pressure. However, the increment of B was larger than that of G , indicating that pressure can effectively improve the ductility of $\text{YBa}_2\text{Cu}_3\text{O}_7$. The quotient of the shear modulus to bulk modulus (G/B) proposed by Pugh [31] was used to predict the brittle or ductile behavior of a solid roughly. A lower (higher) G/B value represents more ductility (more brittleness), and the critical value 0.57 separates the ductile and brittle materials. Figure 3b shows the values of G/B as a function of pressure. The value of G/B decreased automatically with pressure, and all the values were smaller than 0.57, implying that pressure can increase the ductility of $\text{YBa}_2\text{Cu}_3\text{O}_7$; it is ductile itself in the pressure range of 0–100 GPa. In addition, Poisson's ratio $\nu = \frac{3B-2G}{2(3B+G)}$ can also reflect the ductile properties of a material. This ratio usually takes a value from -1 – 0.5 , and it is inversely proportional to G/B . The pressure-dependent ν is also shown in Figure 3b. It can be found that Poisson's ratio ν increases with increasing pressure, and hence, we can obtain the same conclusion from both G/B and ν . Furthermore, all the values of ν were larger than 0.25. $\nu = 0.25$ ($\nu = 0.5$) was

the lower (upper) limit for central force materials. The obtained ν values were all larger than 0.25, which indicates that the interatomic forces in $\text{YBa}_2\text{Cu}_3\text{O}_7$ were predominantly central forces under different pressures.

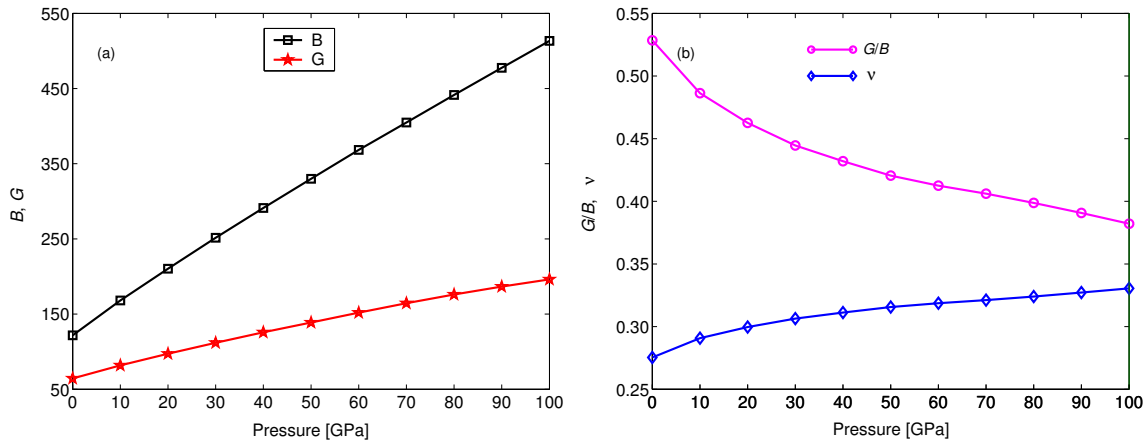


Figure 3. The pressure dependence of (a) bulk modulus B and shear modulus G and (b) the quotient of shear to bulk modulus G/B and Poisson's ratio ν for $\text{YBa}_2\text{Cu}_3\text{O}_7$.

3.2. Elastic Anisotropy of $\text{YBa}_2\text{Cu}_3\text{O}_7$ under Different Pressures

Anisotropy is a key parameter for engineering science, as well as crystal physics, and it is highly correlated with the possibility to induce microcracks in materials [32]. The shear anisotropic factors can be used to measure the directional variability in bonding between atoms in different crystallographic planes. For the orthorhombic $\text{YBa}_2\text{Cu}_3\text{O}_7$, there are three shear anisotropic factors [33,34], i.e., $A_{\{100\}}$ is the shear anisotropic factor along the $\{100\}$ plane between the $\langle 011 \rangle$ and $\langle 010 \rangle$ directions, $A_{\{010\}}$ is the shear anisotropic factor along the $\{010\}$ plane between the $\langle 101 \rangle$ and $\langle 001 \rangle$ directions, and $A_{\{001\}}$ is the shear anisotropic factor along the $\{001\}$ plane between the $\langle 110 \rangle$ and $\langle 010 \rangle$ directions. These shear anisotropic factors can be written as [33]:

$$\begin{aligned} A_{\{100\}} &= \frac{4C_{44}}{C_{11} + C_{33} - 2C_{13}} \\ A_{\{010\}} &= \frac{4C_{55}}{C_{22} + C_{33} - 2C_{23}} \\ A_{\{001\}} &= \frac{4C_{66}}{C_{11} + C_{22} - 2C_{12}} \end{aligned} \quad (5)$$

The shear anisotropy factors $A_{\{100\}}$, $A_{\{010\}}$, and $A_{\{001\}}$ must be one for an isotropic crystal, while any other value smaller or greater than one measures the degree of elastic anisotropy. All the calculated values of various anisotropy factors under pressure up to 100 GPa for $\text{YBa}_2\text{Cu}_3\text{O}_7$ are plotted in Figure 4a. When the applied pressure increased from 0–100 GPa, $A_{\{001\}}$ decreased quickly, but both $A_{\{100\}}$ and $A_{\{010\}}$ had little variation with increasing pressure. $A_{\{001\}}$ firstly decreased from 1.305 to 1.016 and then decreased from 1.016 to 0.758 after 30 GPa, implying that the anisotropy of the $\{001\}$ shear plane between the $\langle 110 \rangle$ and $\langle 010 \rangle$ directions firstly decreased and then increased with pressure. However, pressure had little influence on the shear anisotropy of the $\{100\}$ plane between the $\langle 011 \rangle$ and $\langle 010 \rangle$ directions, as well as the $\{010\}$ plane between the $\langle 101 \rangle$ and $\langle 001 \rangle$ directions. In addition, the percentage elastic anisotropy in compressibility (A_B) and shear (A_G) can be written as follows [35]:

$$\begin{aligned} A_B &= \frac{B_V - B_R}{B_V + B_R} \\ A_G &= \frac{G_V - G_R}{G_V + G_R} \end{aligned} \quad (6)$$

A value of zero represents elastic isotropy, while a value of one refers to the largest possible anisotropy. The pressure dependence of A_B and A_G for $\text{YBa}_2\text{Cu}_3\text{O}_7$ is presented in Figure 4b. It shows that the value of A_G was larger than that of A_B , and the value of A_B was almost close to zero over the whole pressure range investigated, implying that $\text{YBa}_2\text{Cu}_3\text{O}_7$ is largely isotropic in bulk and slightly anisotropic in shear.

To illustrate the elastic anisotropy in detail, it is necessary to investigate the variation of Young's modulus (E) with direction. For orthorhombic crystal, the directional independence of E can be expressed as [33,36]:

$$E^{-1} = s_{11}\alpha^4 + s_{22}\beta^4 + s_{33}\gamma^4 + 2s_{12}\alpha^2\beta^2 + 2s_{23}\beta^2\gamma^2 + 2s_{13}\alpha^2\gamma^2 + s_{44}\beta^2\gamma^2 + s_{55}\alpha^2\gamma^2 + s_{66}\alpha^2\beta^2 \quad (7)$$

where s_{ij} are the elastic compliance constants given by Ney [37] and $\alpha = \sin\theta\cos\varphi$, $\beta = \sin\theta\sin\varphi$, $\gamma = \cos\varphi$ are the direction cosines under the spherical coordinates. The representation surfaces for Young's modulus under different pressures are plotted in Figure 5. Obviously, the representation surfaces for Young's modulus under different pressures deviated in shape from a sphere, and the degree of deviation from the sphere decreased with pressure, indicating that $\text{YBa}_2\text{Cu}_3\text{O}_7$ possessed obvious elastic anisotropy and that the anisotropy of the Young's modulus decreased with pressure. For further comprehensive visualization of the anisotropic features in more detail, the orientation-dependent Young's modulus in the (100), (010), (001), and $(\bar{1}\bar{1}0)$ planes under different pressures are depicted in Figure 6. For the (100) plane, the direction cosines were $\alpha = 0$, $\beta = \sin\theta$, $\gamma = \cos\theta$, and the tensile direction was rotated from [001] to [010]; for the (010) plane, the direction cosines were $\alpha = \sin\theta$, $\beta = 0$, $\gamma = \cos\theta$, and the tensile direction was rotated from [001] to [100]; for the (001) plane, the direction cosines were $\alpha = \cos\theta$, $\beta = \sin\theta$, $\gamma = 0$, and the tensile direction was rotated from [100] to [010]; for the $(\bar{1}\bar{1}0)$ plane, the direction cosines were $\alpha = \frac{a}{\sqrt{a^2+b^2}}\sin\theta$, $\beta = \frac{b}{\sqrt{a^2+b^2}}\sin\theta$, $\gamma = \cos\theta$, and the tensile direction was rotated from [001] to [110]. From Figure 6, we can find that Young's moduli on the researched planes exhibited anisotropy, and the Young's modulus of the (100) plane had a stronger anisotropic character in comparison with other planes under different pressures. The degree of anisotropy in the (010) and $(\bar{1}\bar{1}0)$ planes decreased with pressure, and the Young's modulus of the (010) plane was relatively close to isotropic at 100 GPa. It is clearly visible from Figures 5 and 6 that $\text{YBa}_2\text{Cu}_3\text{O}_7$ was anisotropic under different pressures because of the different bonding characteristics between adjacent atomic planes.

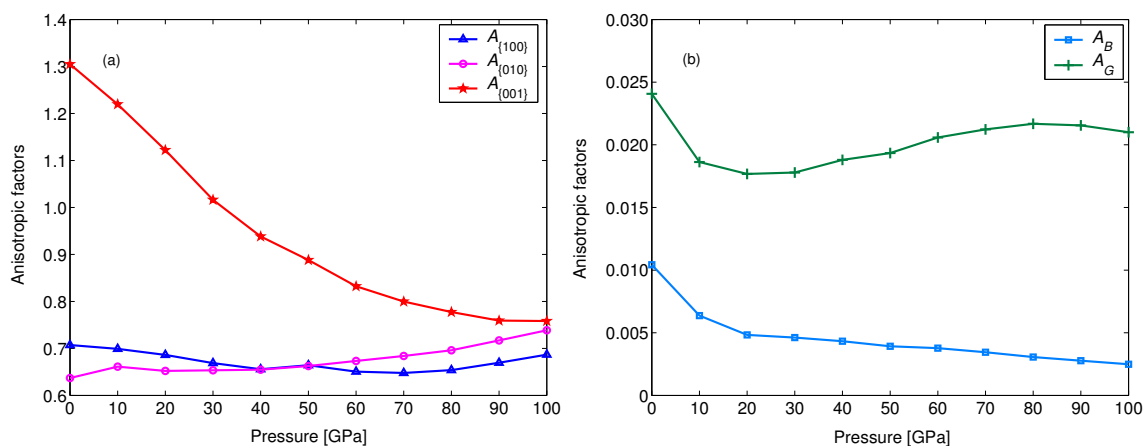


Figure 4. Anisotropic factors (a) $A_{\{100\}}$, $A_{\{010\}}$, and $A_{\{001\}}$ and (b) A_B and A_G of $\text{YBa}_2\text{Cu}_3\text{O}_7$ as a function of pressure.

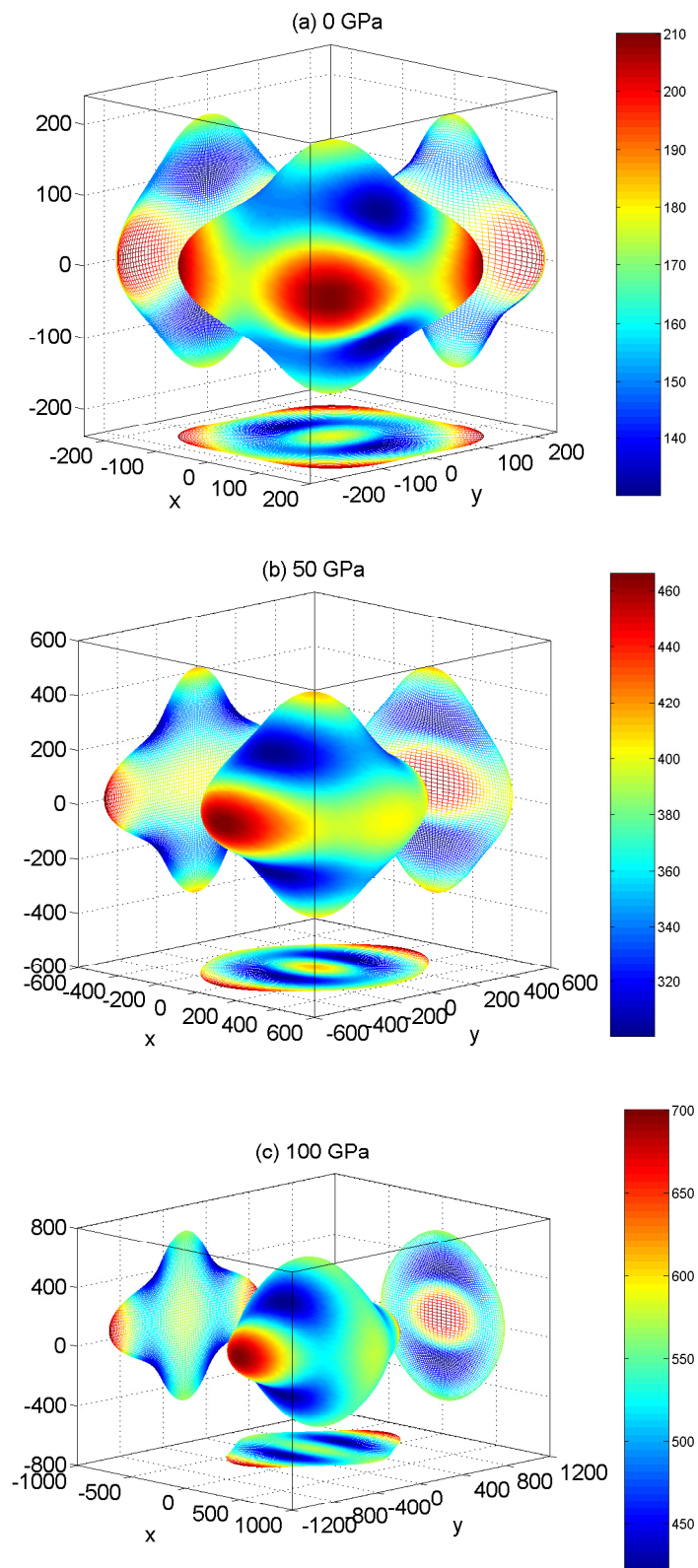


Figure 5. Directional dependence of Young's modulus in $\text{YBa}_2\text{Cu}_3\text{O}_7$ at (a) 0 GPa, (b) 50 GPa and (c) 100 GPa, respectively.

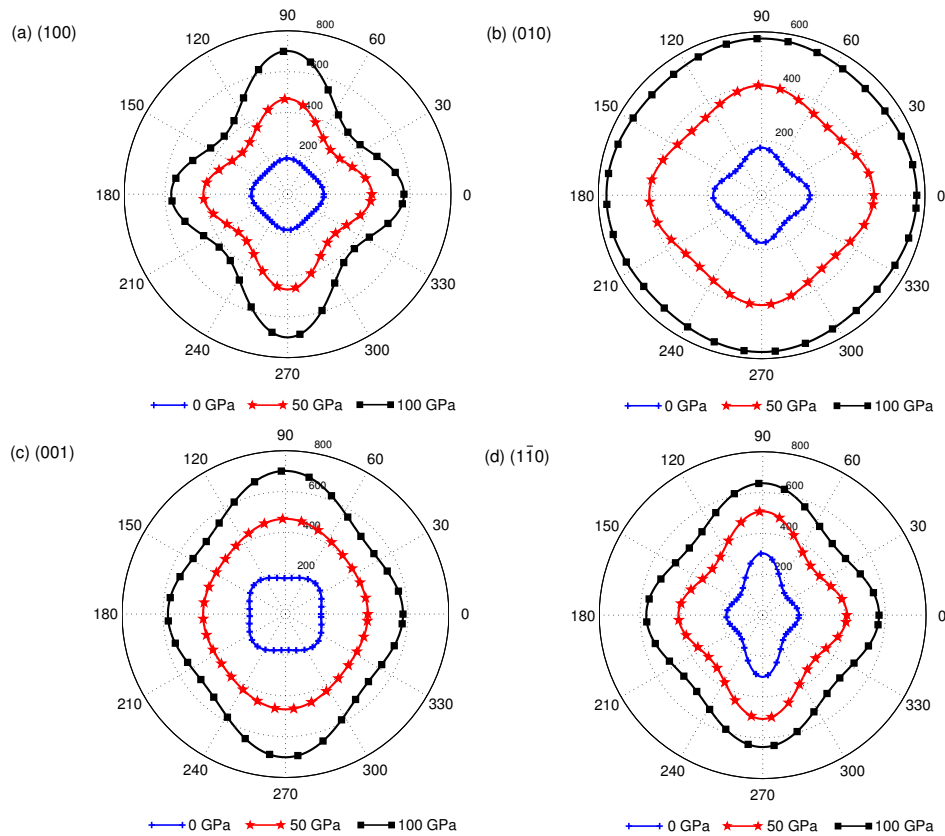


Figure 6. The projections of Young's modulus in the (100) (a), (010) (b), (001) (c), and $(1\bar{1}0)$ (d) planes under different pressures for $\text{YBa}_2\text{Cu}_3\text{O}_7$.

3.3. Thermodynamic Properties of $\text{YBa}_2\text{Cu}_3\text{O}_7$ under Different Pressures

As a fundamental parameter, the Debye temperature Θ_D is closely related to the elastic constants, specific heat, and melting point. At a low temperature, the Debye temperature Θ_D can be deduced from the sound velocities via the following equation [38,39]:

$$\Theta_D = \frac{h}{k_B} \left[\frac{3n}{4\pi} \left(\frac{N_A \rho}{M} \right) \right]^{1/3} v_m$$

$$v_m = \left[\frac{1}{3} \left(\frac{2}{v_s^3} + \frac{1}{v_p^3} \right) \right]^{-1/3}$$

$$v_p = \sqrt{\left(B + \frac{4}{3}G \right) / \rho}$$

$$v_s = \sqrt{G / \rho}$$
(8)

where h is Planck's constant, n is the number of atoms per unit cell, k_B is Boltzmann's constant, M is the molecular weight, N_A is Avogadro's number, ρ is the density, and v_m , v_p , and v_s are the average, longitudinal, and transverse elastic wave velocities, respectively. The calculated sound velocities and Debye temperature as a function of pressure are given in Table 4. The Debye temperature at 0 GPa determined from our elastic constants was 446.34 K, in good agreement with the value 414 K obtained by Lei et al. [29] and the specific heat value 440 K obtained by Inderhees et al. [40]. From Table 4, we can see that all the sound velocities, as well as the Debye temperature increased monotonically with pressure. Since the Debye temperature Θ_D in a solid can describe its covalent strength, the increase of Θ_D with pressure indicated that the covalent strength of $\text{YBa}_2\text{Cu}_3\text{O}_7$ magnified with the increase

of pressure. In general, the higher the Θ_D , the higher the thermal conductivity. Here, the minimum thermal conductivity of $\text{YBa}_2\text{Cu}_3\text{O}_7$ can be evaluated according to Liu's model [41]:

$$k_{\min} = \left\{ \frac{1}{3} \left[2 \left(\frac{1}{2+2\nu} \right)^{-\frac{3}{2}} + \left(\frac{1}{3-6\nu} + \frac{2}{3+3\nu} \right)^{-\frac{3}{2}} \right] \right\}^{-\frac{1}{3}} k_B \sqrt[3]{ \left(\frac{n\rho N_A}{M} \right)^2 \sqrt{\frac{E}{\rho}} } \quad (9)$$

where E is Young's modulus. The calculated minimum thermal conductivities of $\text{YBa}_2\text{Cu}_3\text{O}_7$ under different pressures are also given in Table 4. The value of k_{\min} increased monotonically with pressure, which had the same change trend as Θ_D . Further, $\text{YBa}_2\text{Cu}_3\text{O}_7$ had a very small minimum thermal conductivity ($k_{\min} = 0.863$) at 0 GPa, implying that $\text{YBa}_2\text{Cu}_3\text{O}_7$ was a very competitive candidate material for both an environmental/thermal barrier and oxygen-resistant coating.

Table 4. Calculated shear (v_s), longitudinal (v_p), average (v_m) elastic wave velocities (in m/s), Debye temperature (Θ_D in K), and minimum thermal conductivities (k_{\min} in $\text{W}\cdot\text{m}^{-1}\cdot\text{K}^{-1}$) of $\text{YBa}_2\text{Cu}_3\text{O}_7$ under pressure up to 100 GPa.

P	v_s	v_p	v_m	Θ_D	k_{\min}
0	3228.44	5798.32	3595.06	446.34	0.863
10	3502.94	6449.29	3908.16	497.73	0.987
20	3715.82	6946.87	4150.29	538.54	1.088
30	3892.51	7367.73	4351.39	573.40	1.177
40	4046.44	7728.82	4526.25	604.44	1.257
50	4175.20	8043.70	4672.93	631.51	1.329
60	4300.36	8336.01	4814.94	657.66	1.399
70	4409.75	8591.27	4939.00	681.06	1.463
80	4504.43	8828.15	5046.94	701.93	1.521
90	4583.45	9043.12	5137.59	720.15	1.572
100	4659.65	9241.51	5214.12	736.15	1.619

4. Conclusions

In summary, we investigated the structural stability and mechanical properties of $\text{YBa}_2\text{Cu}_3\text{O}_7$ under pressure up to 100 GPa by means of first principles. It was found that the equilibrium lattice parameters at 0 GPa agreed well with the available experimental data, and $\text{YBa}_2\text{Cu}_3\text{O}_7$ was mechanically stable within 100 GPa. The pressure dependence of Pugh's modulus ratio, Poisson's ratio, elastic anisotropy, Debye temperature, and the minimum thermal conductivity were further investigated for the first time. It was shown that the ductility of $\text{YBa}_2\text{Cu}_3\text{O}_7$ increased monotonically with pressure from both Pugh's modulus ratio and Poisson's ratio. Besides, the Debye temperature and the minimum thermal conductivity increased with pressure, which satisfied the objective rule that the higher the Debye temperature, the higher the minimum thermal conductivity. Due to the relatively lower thermal conductivity of $\text{YBa}_2\text{Cu}_3\text{O}_7$, it is suitable to be used as a thermal insulating material.

Author Contributions: C.C. and L.L. conceived of and designed the theoretical calculations; Y.W. performed the calculations, Y.J. and L.C. analyzed the data; C.C. wrote the paper.

Funding: The work is supported by the Science and Technology Research Program of Chongqing Municipal Education Commission (Grant Nos. KJQN201801211, KJQN201801220), the Natural Science Foundation of China (51661013, 11464020), and the Ph.D. Start-up Fund of the Natural Science Foundation of Jinggangshan University (JZB15007).

Conflicts of Interest: The authors declare no conflict of interest.

References

1. Bednorz, J.G.; Muller, K.A. Possible highTc superconductivity in the Ba-La-Cu-O system. *Z. Phys. B* **1986**, *64*, 189–193. [[CrossRef](#)]
2. Wu, M.K.; Ashburn, J.R.; Torng, C.J.; Hor, P.H.; Meng, R.L.; Gao, L.; Huang, Z.J.; Wang, Y.Q.; Chu, C.W. Superconductivity at 93 K in a new mixed-phase Y-Ba-Cu-O compound system at ambient pressure. *Phys. Rev. Lett.* **1987**, *58*, 908. [[CrossRef](#)] [[PubMed](#)]
3. Mook, H.A.; Yethiraj, M.; Aeppli, G.; Mason, T.E.; Armstrong, T. Polarized neutron determination of the magnetic excitations in YBa₂Cu₃O₇. *Phys. Rev. Lett.* **1993**, *70*, 3490. [[CrossRef](#)] [[PubMed](#)]
4. Ding, F.Z.; Gu, H.W.; Zhang, T.; Wang, H.Y.; Qu, F.; Qiu, Q.Q.; Dai, S.T.; Peng, X.Y.; Cao, J.L. Strong enhancement flux pinning in MOD-YBa₂Cu₃O_{7-x} films with self-assembled BaTiO₃ nanocolumns. *Appl. Surf. Sci.* **2014**, *314*, 622–627. [[CrossRef](#)]
5. Gray, B.A.; Middey, S.; Conti, G.; Gray, A.X.; Kuo, C.T.; Kaiser, A.M.; Ueda, S.; Kobayashi, K.; Meyers, D.; Kareev, M.; et al. Superconductor to Mott insulator transition in YBa₂Cu₃O₇/LaCaMnO₃ heterostructures. *Sci. Rep.* **2016**, *6*, 33184. [[CrossRef](#)] [[PubMed](#)]
6. Horide, T.; Matsukida, N.; Ishimaru, M.; Kita, R.; Awaji, S.; Matsumoto, K. Pin potential effect on vortex pinning in YBa₂Cu₃O_{7-δ} films containing nanorods: Pin size effect and mixed pinning. *Appl. Phys. Lett.* **2017**, *110*, 052601. [[CrossRef](#)]
7. Liu, G.; Zhang, G.; Yu, H.; Jing, L.W.; Ai, L.W.; Liu, Q. Experimental and numerical study of frequency-dependent transport loss in YBa₂Cu₃O_{7-δ} coated conductors with ferromagnetic substrate and copper stabilizer. *J. Appl. Phys.* **2017**, *121*, 243902. [[CrossRef](#)]
8. Murakami, M.; Morita, M.; Koyama, N. Magnetization of a YBa₂Cu₃O₇ Crystal Prepared by the Quench and Melt Growth Process. *Jpn. J. Appl. Phys.* **1989**, *28*, 1189. [[CrossRef](#)]
9. Fong, H.F.; Keimer, B.; Anderson, P.W.; Reznik, D.; Dogan, F.; Aksay, I.A. Phonon and Magnetic Neutron Scattering at 41 meV in YB₂Cu₃O₇. *Phys. Rev. Lett.* **1995**, *75*, 316. [[CrossRef](#)] [[PubMed](#)]
10. Sanchez-Vald'es, C.F.; Puig, T.; Obradors, X. In situ study through electrical resistance of growth rate of trifluoroacetate-based solution-derived YBa₂Cu₃O₇ films. *Supercond. Sci. Technol.* **2015**, *28*, 024006. [[CrossRef](#)]
11. Dadras, S.; Ghavamipour, M. Investigation of the properties of carbon-base nanostructures doped YBa₂Cu₃O_{7-δ} high temperature superconductor. *Physica B* **2016**, *484*, 13–17. [[CrossRef](#)]
12. Horide, T.; Taguchi, K.; Matsumoto, K.; Matsukida, N.; Ishimaru, M.; Mele, P.; Kita, R. Influence of matching field on critical current density and irreversibility temperature in YBa₂Cu₃O₇ films with BaMO₃ (M=Zr, Sn, Hf) nanorods. *Appl. Phys. Lett.* **2016**, *108*, 082601. [[CrossRef](#)]
13. Hapipi, N.M.; Shaari, A.H.; Kechik, M.M.A.; Ban, T.K.; Abd-Shukor, R.; Suib, N.R.M.; Kien, C.S. Effect of Heat Treatment Condition on the Phase Formation of YBa₂Cu₃O_{7-δ} Superconductor. *Solid State Phenom.* **2017**, *268*, 305–310. [[CrossRef](#)]
14. Louail, L.; Maouche, D.; Roumili, A.; Sahraoui, F.A. Calculation of elastic constants of 4d transition metals. *Mater. Lett.* **2004**, *58*, 2975–2978. [[CrossRef](#)]
15. Blochl, P.E. Projector augmented-wave method. *Phys. Rev. B* **1994**, *50*, 17953. [[CrossRef](#)] [[PubMed](#)]
16. Kresse, G.; Joubert, D. From ultrasoft pseudopotentials to the projector augmented wave method. *Phys. Rev. B* **1999**, *59*, 1758. [[CrossRef](#)]
17. Kresse, G.; Hafner, J. Ab initio molecular dynamics for open-shell transition metals. *Phys. Rev. B* **1993**, *48*, 13115. [[CrossRef](#)]
18. Kresse, G.; Furthmüller, J. Efficiency of ab-initio total energy calculations for metals and semiconductors using a plane-wave basis set. *Comput. Mater. Sci.* **1996**, *6*, 15–50. [[CrossRef](#)]
19. Kresse, G.; Furthmüller, J. Efficient iterative schemes for ab initio total-energy calculations using a plane-wave basis set. *Phys. Rev. B* **1996**, *54*, 11169. [[CrossRef](#)]
20. Perdew, J.P.; Burke, K.; Ernzerhof, M. Generalized gradient approximation made simple. *Phys. Rev. Lett.* **1996**, *77*, 3865. [[CrossRef](#)]
21. Monkhorst, H.J.; Pack, J.D. Special points for Brillouin-zone integrations. *Phys. Rev. B* **1976**, *13*, 5188. [[CrossRef](#)]

22. Liu, L.L.; Xu, G.; Wang, A.R.; Wu, X.Z.; Wang, R. First-principles investigations on structure stability, elastic properties, anisotropy and Debye temperature of tetragonal LiFeAs and NaFeAs under pressure. *J. Phys. Chem. Solids* **2017**, *104*, 243–251. [[CrossRef](#)]
23. Voigt, W. *Lehrbuch der Kristallphysik*; Teubner: Stuttgart, Germany, 1928.
24. Reuss, A.; Angew, Z. Berechnung der Fließgrenze von Mischkristallen auf Grund der Plastizitätsbedingung für Einkristalle. *Math. Mech.* **1929**, *9*, 49.
25. Liu, L.L.; Wu, X.Z.; Wang, R.; Nie, X.F.; He, Y.L.; Zou, X. First-Principles Investigations on Structural and Elastic Properties of Orthorhombic TiAl under Pressure. *Crystals* **2017**, *7*, 111. [[CrossRef](#)]
26. Hill, R. The elastic behaviour of a crystalline aggregate. *Proc. Phys. Soc. A* **1953**, *65*, 349. [[CrossRef](#)]
27. Beno, M.A.; Soderholm, L.; Capone, D.W.; Hinks, D.G.; Jorgensen, J.D.; Grace, J.D.; Schuiler, I.K.; Segre, C.U.; Zhang, K. Structure of the single-phase high-temperature superconductor YBa₂Cu₃O_{7-δ}. *Appl. Phys. Lett.* **1987**, *51*, 57–59. [[CrossRef](#)]
28. Cava, R.J.; Batlogg, B.; vanDover, R.B.; Murphy, D.W.; Sunshine, S.; Siegrist, T.; Remeika, J.P.; Reitman, E.A.; Zahurak, S.; Espinosa, G.P. Bulk Superconductivity at 91 K in Single-Phase Oxygen-Deficient Perovskite Ba₂YCu₃O_{9-δ}. *Phys. Rev. Lett.* **1987**, *58*, 1676. [[CrossRef](#)]
29. Lei, M.; Sarrao, J.L.; Visscher, W.M.; Bell, T.M.; Thompson, J.D.; Migliori, A. Elastic constants of a monocrystal of superconducting YBa₂Cu₃O_{7-δ}. *Phys. Rev. B* **1993**, *47*, 6154. [[CrossRef](#)]
30. Sin'ko, G.V.; Smirnov, N.A. Ab initio calculations of elastic constants and thermodynamic properties of bcc, fcc, and hcp Al crystals under pressure. *J. Phys. Condens. Matter* **2002**, *14*, 6989.
31. Pugh, S.F. Relations between the elastic moduli and the plastic properties of polycrystalline pure metals. *Philos. Mag.* **1954**, *45*, 823–843. [[CrossRef](#)]
32. Tvergaard, V.; Hutchinson, J.W. Microcracking in Ceramics Induced by Thermal Expansion or Elastic Anisotropy. *J. Am. Ceram. Soc.* **1988**, *71*, 157–166. [[CrossRef](#)]
33. Ravindran, P.; Fast, L.; Korzhavyi, P.A.; Johansson, B.; Wills, J.; Eriksson, O. Density functional theory for calculation of elastic properties of orthorhombic crystals: Application to TiSi₂. *J. Appl. Phys.* **1998**, *84*, 4891–4904. [[CrossRef](#)]
34. Miao, N.X.; Pu, C.Y.; He, C.Z.; Zhang, F.W.; Lu, C.; Lu, Z.W.; Zhou, D.W. Mechanical and thermodynamic properties of the monoclinic and orthorhombic phases of SiC₂N₄ under high pressure from first principles. *Chin. Phys. B* **2014**, *23*, 127101. [[CrossRef](#)]
35. Chung, D.H.; Buessem, W.R. The elastic anisotropy of crystals. *J. Appl. Phys.* **1967**, *38*, 2010–2012. [[CrossRef](#)]
36. Wei, Q.; Zhang, M.G.; Guo, L.X.; Yan, H.Y.; Zhu, X.M.; Lin, Z.Z.; Guo, P. Ab initio studies of novel carbon nitride phase C₂N₂(CH₂). *Chem. Phys.* **2013**, *415*, 36–43. [[CrossRef](#)]
37. Nye, J.F. *Physical Properties of Crystals: Their Representation by Tensors and Matrices*; Oxford University Press: New York, NY, USA, 1985.
38. Anderson, O.L. A simplified method for calculation of the Debye temperature from elastic constants. *J. Phys. Chem. Solids* **1963**, *24*, 909–917. [[CrossRef](#)]
39. Schreiber, E.; Anderson, O.L.; Soga, N. *Elastic Constants and Their Measurements*; McGraw: New York, NY, USA, 1973.
40. Inderhees, S.; Salamon, M.; Friedmann, T.; Ginsberg, D.M. Measurement of the specific-heat anomaly at the superconducting transition of YBa₂Cu₃O_{7-δ}. *Phys. Rev. B* **1987**, *36*, 2401. [[CrossRef](#)]
41. Liu, B.; Wang, J.Y.; Li, F.Z.; Zhou, Y.C. Theoretical elastic stiffness, structural stability and thermal conductivity of La₂Ta₂O₇ (T=Ge, Ti, Sn, Zr, Hf) pyrochlore. *Acta Mater.* **2010**, *58*, 4369–4377. [[CrossRef](#)]

